Energy Materials and Devices

Research Article

# Facile modification using organic acid molecules to neutralize residual alkaline compounds for stabilizing $LiNi_{0.95}Co_{0.04}Mn_{0.01}O_2$ cathode material

Chao Zhao, Xiangshao Yin, Yuanyuan Huang, Xinyu Zhang, Weihong Jiang, Zhuo Zhou, Wenhui Tu, Xianshu Wang ✉, Ding Wang ✉, and Jianguo Duan ✉

## Graphical Abstract

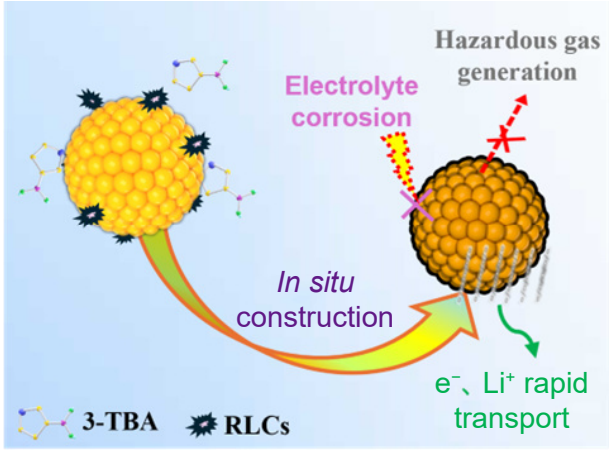


Herein, we propose neutralizing residual alkaline compounds on the surface of $LiNi_{0.95}Co_{0.04}Mn_{0.01}O_2$ (NCM) cathode material using 3-thiopheneboronic acid (3-TBA), a facile strategy for improving the performance of the cathode material without any posttreatments. The formed thin and uniform interface stabilizes the cathode material by suppressing unfavorable phase transitions, reducing carbon dioxide ($CO_2$) gas evolution, and mitigating electrolyte decomposition, thereby improving the electrochemical performance and safety of the battery.

✉Address correspondence to Xianshu Wang, xswang2016@m.scnu.edu.cn; Ding Wang, wangding@kust.edu.cn; Jianguo Duan, duanjianguo@kmust.edu.cn

**Received:** December 26, 2024
**Revised:** February 6, 2025
**Accepted:** February 14, 2025



**Citation:** Zhao C., Yin X., Huang Y., et al. Facile modification using organic acid molecules to neutralize residual alkaline compounds for stabilizing $LiNi_{0.95}Co_{0.04}Mn_{0.01}O_2$ cathode material. *Energy Mater. Devices*, 2025, 3(1), 9370056. https://doi.org/10.26599/EMD.2025.9370056

Energy Materials and Devices

Open Access

Research Article

https://doi.org/10.26599/EMD.2025.9370056

# Facile modification using organic acid molecules to neutralize residual alkaline compounds for stabilizing $LiNi_{0.95}Co_{0.04}Mn_{0.01}O_2$ cathode material

Chao Zhao[1,2], Xiangshao Yin[1], Yuanyuan Huang[1], Xinyu Zhang[1], Weihong Jiang[1], Zhuo Zhou[1], Wenhui Tu[1], Xianshu Wang[1] ✉, Ding Wang[1] ✉, and Jianguo Duan[1] ✉

[1] *Key Laboratory of Advanced Battery Materials of Yunnan Province, National and Local Joint Engineering Research Center of Lithium-ion Batteries and Materials Preparation Technology, School of Metallurgical and Energy Engineering, Kunming University of Science and Technology, Kunming 650093, China*

[2] *School of Materials Science and Engineering, Central South University, Changsha 410083, China*

**Received:** December 26, 2024 / **Revised:** February 6, 2025 / **Accepted:** February 14, 2025

## ABSTRACT

The presence of residual alkaline compounds in the ultrahigh-nickel layered oxide cathodes ($LiNi_xCo_yMn_{1-x-y}O_2$, $x \geq 0.9$) aggravates structural degradation, increases surface reactivity, and promotes slurry gelation, leading to the capacity decay of batteries with these cathodes and complicating their manufacturing. Traditional approaches for addressing this issue, including direct removal, coverage, and utilization, are complex and require surface regeneration. Herein, we propose neutralizing residual alkaline compounds with 3-thiopheneboronic acid (3-TBA) to improve the performance of $LiNi_{0.95}Co_{0.04}Mn_{0.01}O_2$ (NCM) cathode material, a facile strategy that does not require any post-treatment. The suggested reaction yields a uniform and thin organic-modified layer on the surface of the NCM cathode, improving its chemical stability toward the electrolyte, as demonstrated by multiple characterization methods. The modified NCM cathode exhibited impressive cyclic and rate performances, achieving a capacity retention of 83.34% after 200 cycles at 1.0 C and a specific capacity of 162.00 mAh·g$^{-1}$ at 10.0 C. Most importantly, the proposed approach can efficiently suppress unfavorable phase transitions, severe electrolyte degradation, and $CO_2$ gas evolution, improving the application potential of ultrahigh-nickel layered oxide cathode materials.

## KEYWORDS

lithium-ion battery, ultrahigh-nickel layered oxide cathode, residual alkaline compounds, organic molecule, neutralization

## 1 Introduction

Lithium-ion ($Li^+$) batteries have served as the crucial link for the development of new energy technologies in recent years, particularly in electric vehicles, consumer electronics, and grid storage, leading to a substantial demand for batteries with high energy density and long cycle life. Ultrahigh-nickel layered oxides ($LiNi_xCo_yMn_{1-x-y}O_2$, $x \geq 0.9$) stand out from many other cathode materials owing to their high discharge specific capacity (>200.00 mAh·g$^{-1}$) and high operating voltage (>3.80 V vs. Li/$Li^+$), thus, they have been widely adopted in the energy sector. However, the increase in Ni content in the bulk leads to an increase in the amount of surface alkaline residuals, increasing surface reactivity and anisotropic unit-cell volume variation, which is detrimental to both the battery capacity and cycling stability. Residual Li compounds (RLCs) generally refer to amorphous Li-containing surface impurities, such as LiOH, $LiHCO_3$, and $Li_2CO_3$[1,2], attached to the surface of high-nickel cathode materials[3]. RLCs are

✉Address correspondence to Xianshu Wang, xswang2016@m.scnu.edu.cn; Ding Wang, wangding@kust.edu.cn; Jianguo Duan, duanjianguo@kmust.edu.cn

generated owing to the excessive addition of Li precursors during material synthesis, resulting in the formation of $Li_2O$ from unreacted Li residuals on the material surface. Chemically reactive $Li_2O$ interacts with environmental carbon dioxide ($CO_2$) and $H_2O$, forming LiOH, $LiHCO_3$, and $Li_2CO_3$. The presence of Li impurities not only escalates the storage costs[4] but also induces slurry gelation during preparation. Additionally, the intrinsic insulating effect of RLCs increases the interfacial resistance ($R_i$) to $Li^+$ shuttling. Therefore, RLCs, which alter the surface properties, impact the electrochemical performance, and lead to inadequate cycle life of high-nickel cathodes, must be removed from the surface of cathode materials.

Traditional strategies for addressing this issue mainly include direct removal, surface coverage, and rational utilization[5–8]. In direct removal, alkaline components are removed through water/alcohol washing or gas-phase heat treatment. Unfortunately, washing makes cathode materials more sensitive to air, leading to increased cation–anion dislocation[9,10]. At the same time, annealing in air at >400 °C tends to compromise the structural integrity and capacity delivery of cathode materials. In the surface coverage approach, a physical contact inhibitor is constructed by coating cathode materials with compounds such as oxides or fluorides to shield them against electrolyte erosion and sustain their structural stability to some extent. Despite this, these compounds, possessing high intrinsic bulk and $R_i$, tend to enhance battery polarization and reduce $Li^+$ diffusivity. At the same time, in rational utilization, RLCs are eliminated through reactions with external reagents. After roasting, the pre-reacted products further become the featured components of protective surface/interface layer. For instance, Seong et al.[11] have induced the preferential conversion of residual $Li_2O$ in $LiNi_{0.91}Co_{0.06}Mn_{0.03}O_2$ into a $Li_2SO_4$ film by injecting sulfur dioxide ($SO_2$) gas during calcination. This approach has been found to suppress the formation of RLCs during synthesis and storage, alleviating slurry gelation and gas evolution during battery charging/discharging. Given the complexity of this long-term process, a facile solution for curing RLCs must be developed to maintain the structural integrity and simultaneously improve capacity retention.

In this context, an innovative approach with comparative convenience has been developed to significantly improve the electrochemical stability of the $LiNi_{0.95}Co_{0.04}Mn_{0.01}O_2$ (NCM) cathode material. This strategy consists of the neutralization of RLCs with 3-thiopheneboronic acid (3-TBA), allowing to modify the surface of NCM without the tedious pretreatment. As shown in Fig. 1a, the boronic acid group (–B–O–H) in 3-TBA reacts with the hydroxyl or carbonate groups in RLCs, leading to the chemical bonding of 3-TBA with the NCM surface. Such a facile modification approach ensures good $Li^+$ conductivity and reduces the surface reactivity, volume variation, and gas evolution of the cathode material. Consequently, the cell with the modified NCM cathode (NCM@TBA) exhibited superior high-rate specific capacity and cycling stability, accompanied by excellent $Li^+$ diffusion and suppressed gas evolution compared to the control sample. This work underscores the efficacy of "soft chemistry" for improving the mechanical and electrochemical stability of electrode materials, providing a novel approach for the removal of RLCs from the surface of ultrahigh-nickel layered oxide cathode materials.

## 2 Materials and methods

### 2.1 Materials preparation

NCM cathode material was synthesized using solid-phase sintering. First, 100.00 g of the hydroxide precursor, $Ni_{0.95}Co_{0.04}Mn_{0.01}(OH)_2$ (Guangzhou Libond New Material Co., Ltd.), was calcinated at 480 °C for 5.0 h in an oxygen atmosphere, after which the oxidized precursor was mixed with $LiOH{\cdot}H_2O$ (45.38 g, analytically pure, Aladdin's Reagent, Inc.) via ball milling for 1.5 h. Finally, the uniform mixtures were pretreated at 480 °C for 4.0 h and calcined at 750 °C for 12.0 h in an oxygen atmosphere in a tube furnace. 3-TBA (5.00 g, $M_w$ = 127.96, analytically pure) was purchased from Rhawn's Reagent, Inc.

NCM was modified with 3-TBA through the wet chemical method as follows. (1) Cathode material dispersion: 10.00 g of NCM was added to 50 mL of ethylene glycol and continuously stirred at room temperature until a uniform suspension (Suspension A) was obtained. (2) Dissolution of organic boric acid: 0.02 g of 3-TBA was accurately weighed and added to 5 mL of ethylene glycol, followed by thorough stirring for 1.0 h to obtain a homogeneous transparent solution (Solution B). (3) Spray drying to form an artificial cathode–electrolyte interphase: The employed spray dryer was preheated to the set temperature while ensuring that the machine chamber was completely dry. A certain amount of Solution B was precisely measured and added dropwise to Suspension A under vigorous stirring, followed by continuous stirring for 1.0 h. The solvent was removed via spray drying at 180 °C and a rate of 10 $mL{\cdot}min^{-1}$. The as-sprayed material was further dried in a vacuum oven at 120 °C for 12.0 h, yielding a high-nickel cathode material with an artificial cathode–electrolyte interphase layer. The synthesis diagram is shown in Fig 1a.

### 2.2 Physical characterizations

The crystalline structures of the samples were charac-

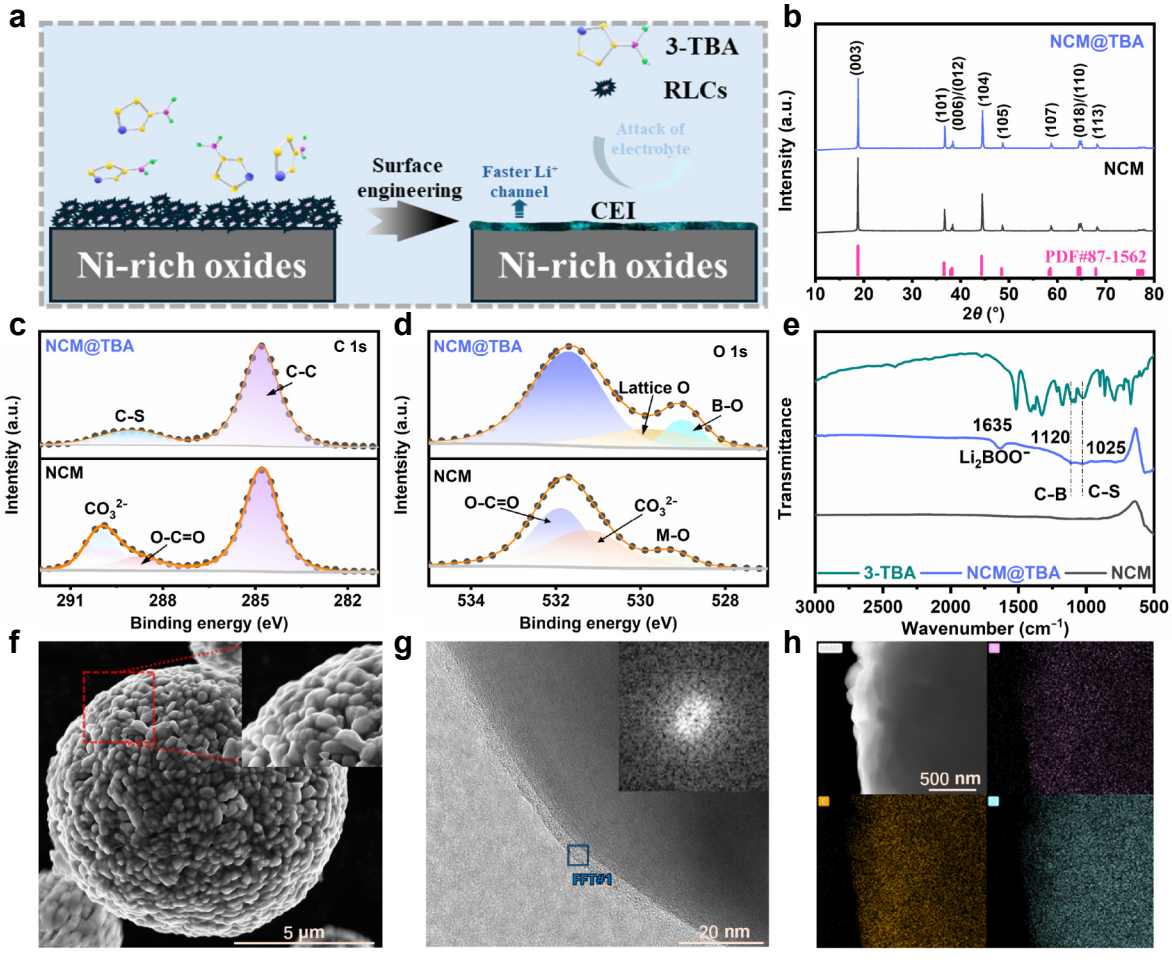


**Figure 1** Characterizations of NCM@TBA. (a) Schematic of the synthesis route of NCM@TBA. (b) XRD patterns of NCM and NCM@TBA. C 1s (c) and O 1s (d) XPS spectra of NCM and NCM@TBA. (e) Fourier transform infrared spectra of 3-TBA, NCM, and NCM@TBA. (f) SEM images of NCM@TBA. TEM (g) and high-resolution TEM (h) images of NCM@TBA with EDS maps of B, C, and S; inset in (g) are the corresponding fast Fourier transform images.

terized via powder X-ray diffraction (XRD; Rigaku SmartLab, Japan) at a scanning rate of 5 °·min$^{-1}$ using Cu K$\alpha$ radiation. *In situ* XRD patterns were acquired to survey the phase change of the samples during the first charge–discharge cycle. The morphology of all samples was observed using scanning electron microscopy (SEM; Thermo Fisher FEI Nova-Nano 450, USA), and transmission electron microscopy (TEM; FEI Talos F200X G2, USA) coupled with energy dispersive spectroscopy (EDS) to determine particles size, surface structure, and coating thickness. The chemical bonds between NCM and 3-TBA in NCM@TBA were detected using X-ray photoelectron spectroscopy (XPS; Thermo Fisher Scientific ESCALAB Xi$^+$, USA) with monochromatized Al K$\alpha$ radiation ($h\upsilon$ = 1486.60 eV, where $h$ is Planck's constant, and $\upsilon$ is the frequency), electron emission angle of 45°, and an analysis area size of 650 μm. The sample was not sputter-etched before analysis. During operation, the base pressure was $10^{-8}$ mbar, and the charge neutralizer was not used. Time-of-flight second ion mass spectroscopy (TOF-SIMS) measurements were performed on a Nano TOF-2 instrument (ULVAC-PHI, Japan) equipped with a $Bi^{3+}$ beam (30 kV) cluster primary-ion gun for analysis and an argon-ion ($Ar^+$) beam (3 keV and 100 nA) with a sputtering rate of 0.1 nm·s$^{-1}$ to obtain the desired depth profile. The area of analysis was 100 μm × 100 μm, whereas the sputtering area was 400 μm × 400 μm.

## 2.3 Electrochemical measurements

Working electrodes were prepared by coating a mixed slurry consisting of 94.0 wt.% active material (NCM and NCM@TBA), 3.0 wt.% Super P, and 3.0 wt.% polyvinylidene fluoride onto Al foil, followed by drying at 120 °C. The areal loading of the cathode materials was 10 mg·cm$^{-2}$. Half-cells were assembled in a glove box filled with Ar gas, with metallic Li as the counter electrode and reference electrodes and a 1 mol·L$^{-1}$ solution of $LiPF_6$ in EC:DMC:EMC (1:1:1, by volume) as the electrolyte. The cycling performance was assessed using a battery testing system (Land CT-2001A, China) in the poten-

tial range of 2.80–4.30 V (vs. Li/Li$^+$). Cyclic voltammetry (CV) was conducted on an electrochemical workstation (Bio-Logic VMP3, France). Electrochemical impedance spectroscopy (EIS) was performed on an electrochemical workstation (Metrohm, Autolab PGSTAT302N, Switzerland) in the frequency range of 100 kHz–0.01 Hz with an amplitude of 5.0 mV. Galvanostatic intermittent titration technique (GITT) tests were performed on a battery testing system (Land CT3002A, China), and the Li$^+$ diffusion coefficient ($D_{Li^+}$) of the samples was calculated using Eq. (1)[12,13] as follows

$$D_{Li^+} = \frac{4}{\pi\tau}\left(\frac{m_B V_m}{M_B S}\right)^2\left(\frac{\Delta E_s}{\Delta E_\tau}\right)^2 \quad (1)$$

where $\tau$ is the relaxation time, $m_B$ and $M_B$ are the molecular weight and mass of the cathode material, respectively, $V_m$ is the molar volume of NCM, $S$ is the active surface area of the electrode, and $\Delta E_s$ and $\Delta E_\tau$ are the steady-state relaxation voltage change and the instantaneous voltage change at the end of the pulse, respectively.

## 3 Results and discussion

The modification effect of 3-TBA on NCM was assessed based on changes in the morphology, structure, and surface properties. As shown in Fig. 1b, similar diffraction peaks appear in both the NCM and NCM@TBA samples. These peaks correspond to layered hexagonal $NaFeO_2$ (PDF#87-1562)[14] with the R3m space group, indicating that the typical layered structure is preserved after modification with 3-TBA. This is further confirmed by the rendered (006)/(012) and (018)/(110) pairs of splitting peaks[15].

XPS was conducted to analyze the changes in NCM after the treatment with 3-TBA. The positions of the characteristic peaks of Co 2p and Mn 2p are almost unchanged after modification (Fig. S1 in Supplementary Material). However, the intensity of these peaks is slightly lower in the NCM@TBA sample than in the NCM sample. This decrease was attributed to the shielding effect of the coating layer and indirectly suggests the successful fixation of 3-TBA on the surface of NCM. The same trend is observed in the Ni 2p spectra (Fig. S2a in Supplementary Material), showing two dominant peaks at 855.10 and 856.30 eV assigned to $Ni^{2+}$ and $Ni^{3+}$[16], respectively. The similar relative contents of $Ni^{2+}/Ni^{3+}$ indicate that the formed organic layer has a negligible effect on Ni. Additionally, the C 1s spectrum of the NCM sample shows the characteristic peaks of C–C and O–C=O at 284.80 and 288.70 eV[17] (Fig. 1c), respectively, as well as a distinct $CO_3^{2-}$ peak at 290.10 eV[18], indicating the significant presence of $Li_2CO_3$ (one of RLCs). At the same time, in addition to the similar C–C bond, a C–S bond (289.00 eV) was detected in the C 1s spectrum of the NCM@TBA sample. This signal is further reflected in the characteristic peak of $-(C_4H_2S)_x-$ at 163.90 eV[19] in the S 2p spectrum (Fig. S2c in Supplementary Material). Notably, an additional peak at 168.00–172.00 eV, corresponding to thiosulfate ($SO_x^{2-}$)[20], appears in the two samples, which was attributed to the residual sulfate remaining after coprecipitation. The O 1s spectra further confirm the presence of RLCs on the surface of NCM and the neutralization of RLCs with 3-TBA. In the O 1s spectra, three characteristic peaks of O–C=O at 531.80 eV, $CO_3^{2-}$ at 531.20 eV, and M–O at 528.80 eV are observed for the NCM sample, whereas the $CO_3^{2-}$ peak is not observed for the NCM@TBA sample (Fig. 1d), consistent with the C 1s spectra. Moreover, the characteristic peak of B–O at 529.10 eV is observed only for NCM@TBA. The signals of B-containing groups are also observed in the Li 1s spectrum (Fig. S2b in Supplementary Material) as the peaks of $(Li_2O)_x(B_2O_3)_{1-x}$[21] and $LiBO_2$ at 55.40 and 53.90 eV, respectively. By comparison, the NCM sample shows only a characteristic peak of $Li_2CO_3$ at 55.20 eV in the Li 1s spectrum, indicating the presence of RLCs. In the B 1s spectra, no B signal is detected for the NCM sample, whereas a characteristic B–Li peak is detected at 192.02 eV for NCM@TBA. The above results suggest that these B and S signals are derived from the –B–OH and thiophene groups in 3-TBA. Furthermore, the results of Fourier transform infrared spectroscopy, confirm the presence of feature elements after neutralization (Fig. 1e), with the peaks of C–B stretching vibration and C–S torsion observed at 1120 and 1025 cm$^{-1}$.

SEM was used to observe the changes in the morphology of NCM after modification with 3-TBA. NCM consists of spherical particles with a diameter of 10 μm, composed of nanoscale primary particles with sharp edges (Fig. S3a in Supplementary Material). The enlarged view reveals the presence of black-gray particles adhering to the surface of NCM particles (Fig. S3b in Supplementary Material), which are the surface alkaline Li compounds[22]. However, after modification, the NCM@TBA particles are smooth, with a thin transparent protective layer uniformly coating the surface of the primary particles (Fig. 1f and its inset). The surface morphology and microstructure of the materials were further characterized using TEM, selected area electron diffraction, and EDS. As shown in Fig. S4 in Supplementary Material, the NCM cathode material has a rough surface, indicating the presence of RLCs and providing a solid foundation for subsequent modifications. Notably, Ni, Co, Mn, and O are uniformly distributed throughout the material, without significant enrichment or depletion[23]. At the same time, the surface of the NCM@TBA cathode material is round and smooth (Fig. 1f and its inset). Its TEM

image reveals the presence of a uniform film with a thickness of approximately 3–4 nm (Fig. 1g), which is not observed on the surface of pristine NCM. Fast Fourier transform images indicate that this surface layer is amorphous, contrasting with the lattice fringes in the bulk. Such uniform and thin layers are also observed in the NCM samples modified with different amounts of 3-TBA (Figs. S5a and S5b in Supplementary Material). Figure 1h and Figs. S5c and S5d in Supplementary Material show that S, C, and B are uniformly distributed in NCM@TBA, suggesting the uniform coating with 3-TBA.

To assess the stability of the modified layer, NCM and NCM@TBA electrodes with a diameter of 12 mm were prepared and assembled into coin cells with a Li metal anode, followed by resting at 25 °C for 12.0 h to ensure thorough contact with the carbonate electrolyte. Subsequently, the electrodes were removed under an Ar atmosphere for testing via TOF-SIMS. The changes in the surface composition of the material after modification were analyzed using the obtained three-dimensional (3D) surface reconstructions. As shown in Figs. 2a–2c, within a sputtering depth of 40 nm, considerable accumulation and deep penetration of $C_2H_2O^-$ and $C_2H_3O^-$ species are observed on the surface of the pristine NCM electrode, along with a noticeable $PO_2F_2^-$ signal in the surface layer. The first two species are generally known as the by-products of solvent decomposition, whereas the latter originates from the hydrolysis/pyrolysis of $LiPF_6$[24]. This indicates that RLCs induce spontaneous side reactions. In contrast, because of the elimination of RLCs and the presence of the organic-modified layer, the signals of these species in the interior of the NCM@TBA cathode material are substantially weaker (Figs. 2d–2f), suggesting reduced electrolyte decomposition during resting and greatly enhanced chemical stability of the cathode material and its interface.

The electrochemical performance of NCM@TBA cathodes was extensively studied in coin cells using a Li metal counter electrode over a voltage range of 2.80–4.30 V (vs. $Li/Li^+$). To obtain optimal results, the initial charge/discharge specific capacity at 0.1 C (1.0 C = 210 $mA{\cdot}g^{-1}$) and the cycling stability at 1.0 C were determined for cells with the pristine NCM cathode or NCM cathodes modified with various amounts of 3-TBA (Figs. 3a and 3b). The cell with the pristine NCM cathode shows an initial charge/discharge specific capacity of 249.00/222.70 $mAh{\cdot}g^{-1}$, slightly outperforming the Li‖NCM@TBA cell (239.80/220.30 $mAh{\cdot}g^{-1}$), as shown in Fig. 3a. The slightly lower specific capacity of the latter was attributed to the intrinsic internal impedance of the modified layer. However, the cell with the modified cathode shows higher Coulombic efficiency (CE) than the cell with the unmodified cathode, 91.87% and 89.44%, respectively. The other modified samples also exhibit high initial CEs, reaching 90.46% (NCM@TBA-0.5 wt.%) and 90.71% (NCM@TBA-1.5 wt.%). These results indicate that RLCs affect the CE during the initial charge/discharge. Figure 3b shows the electrochemical cyclic performance of the cells at 1.0 C, indicating superior capacity retention of the cells with modified cathodes. Specifically, after 200 cycles, the cell with the pristine NCM cathode exhibits a capacity retention rate of 66.91%, whereas the Li‖NCM@TBA cell shows a capacity retention rate of 83.34% (superior to the other two variations, which exhibit 76.38% and 77.28%). To evaluate the rate performance of the NCM and NCM@TBA cathodes, constant current charge/discharge tests were conducted on the assembled coin cells at current rates of 0.1–10.0 C. The Li‖NCM@TBA cell shows stable reversible discharge specific capacities of 224.30, 220.40, 215.60, 208.90,

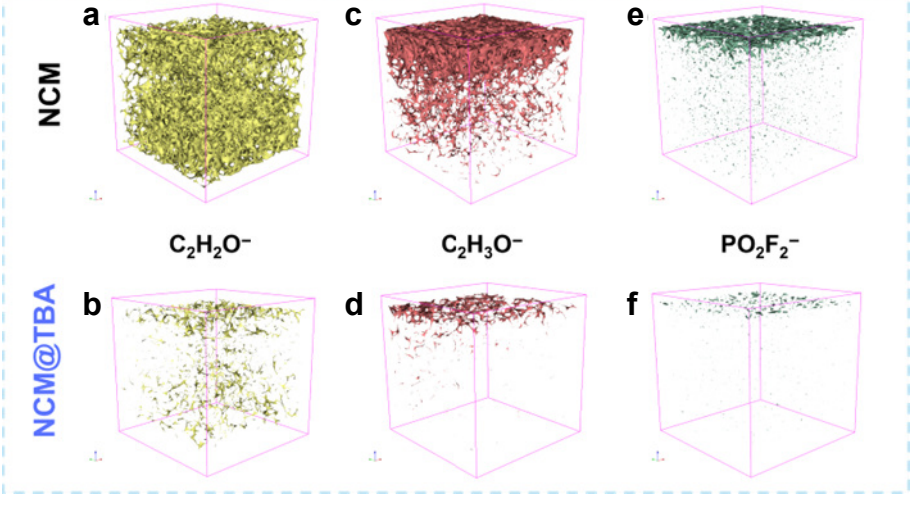


**Figure 2** 3D reconstructions of $C_2H_2O^-$ (a, b), $C_2H_3O^-$ (c, d), and $PO_2F_2^-$ (e, f) in the NCM and NCM@TBA electrodes after the contact with the electrolyte but before cycling.

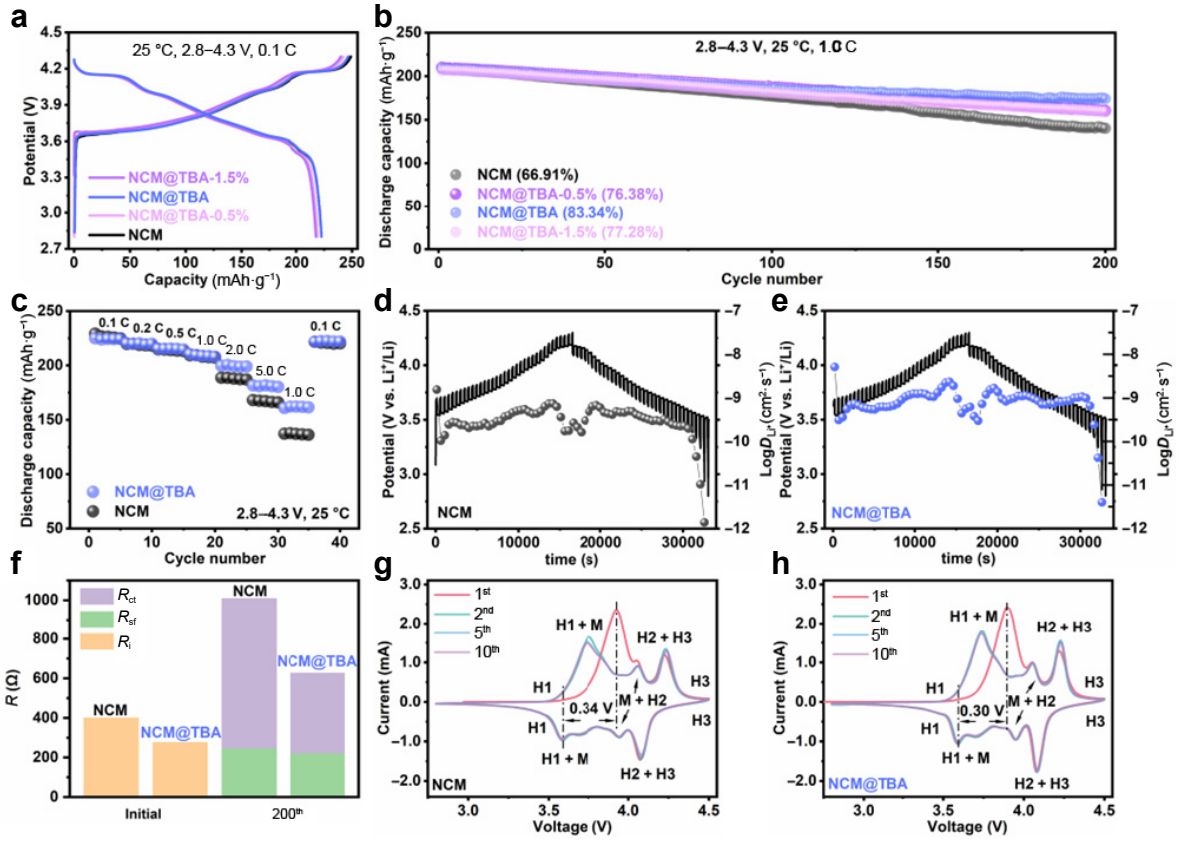


**Figure 3** Electrochemical performance. Initial charge/discharge curves (a), cycling stability (b), rate capabilities (c), and ion diffusion coefficients (d, e) determined via GITT of the Li‖NCM and Li‖NCM@TBA cells. (f) Impedances of Li‖NCM and Li‖NCM@TBA cells before cycling and after 200 cycles. (g, h) CV curves of the Li‖NCM and Li‖NCM@TBA cells.

199.30, 181.70, and 162.60 mAh·g$^{-1}$ at current densities of 0.1, 0.2, 0.5, 1.0, 2.0, 5.0, and 10.0 C, respectively (Fig. 3c). At the same time, the Li‖NCM cell shows worse fast-charge/discharge capabilities, with discharge specific capacities of 226.30, 219.90, 214.60, 209.50, 187.90, 167.10, and 137.80 mAh g$^{-1}$, respectively. At low current densities, the discharge specific capacities of both materials are similar. However, with the increase in current density from 2.0 to 10.0 C, the difference in the discharge specific capacities between the two materials becomes more pronounced, with the Li‖NCM and Li‖NCM@TBA cells showing specific capacities of 136.21 and 162.27 mAh·g$^{-1}$ at 10.0 C, respectively. These results indicate the NCM@TBA cathode can endow the cell with enhanced fast-charge/discharge performance.

Such a good fast-charge/discharge capacity may imply enhanced kinetic behavior, therefore, GITT measurements were performed. $D_{Li^+}$, derived from the GITT curves, are presented on a logarithmic scale for clarity. Figures 3d and 3e show that the log$D_{Li^+}$ value of NCM@TBA (−8.9 cm$^2$·s$^{-1}$) is notably larger than that of NCM (−9.6 cm$^2$·s$^{-1}$), suggesting the better $Li^+$ diffusivity of NCM@TBA. This was attributed to the good $Li^+$ conductivity of the as-formed B-/S-containing heterogeneous components on the cathode surface[25,26]. EIS was performed to determine the impedance of the cells with the NCM and NCM@TBA cathodes before cycling and after 200 cycles (Fig. 3f). The Nyquist plots and the corresponding equivalent short circuits suggest that before cycling, the fitted values of $R_i$ for the Li||NCM and Li||NCM@TBA cells are 384.0 and 261.0 Ω (Fig. S6 in Supplymentary Material), respectively. The higher $R_i$ of the Li||NCM cell was ascribed to the reservation of RLCs and their spontaneous side reactions. After 200 cycles, the first semicircle associated with the resistance of the surface film ($R_{sf}$) at high frequencies for the Li||NCM@TBA cell is slightly smaller than that for the cell with the NCM cathode (227.6 vs. 241.2 Ω). The second semicircle, corresponding to the charge-transfer resistance ($R_{ct}$) at middle frequencies, considerably differs between the cells. The $R_{ct}$ value of the cell with the NCM cathode was estimated at 811.5 Ω, which was notably lower than that of the cell with the NCM@TBA cathode (385.8 Ω), revealing that the proposed modification effectively limited the thickening of the surface film and continuous electrolyte decomposition caused by RLCs.

CV was employed to study the electrochemical redox reactions in the cells with the NCM and NCM@TBA cathodes[27,28]. Figures 3g and 3h show the CV plots for the cells with the NCM and NCM@TBA cathodes during the first, second, fifth,

and tenth cycles at a scan rate of 0.1 mV·s$^{-1}$ within the voltage range of 2.80–4.50 V. During the first charge, three pairs of redox peaks are observed for both the NCM and NCM@TBA cathodes, which correspond to the H1→M, M→H2, and H2→H3 phase transitions[29]. The redox curves for both overlap well in subsequent cycles, apart from an oxidation peak at high potential and a reduction peak at low potential in the initial cycle. This difference between the initial and subsequent cycles was attributed to the irreversible capacity loss caused by the formation of the surface film and the consumption of $Li^+$ during the first charge, which is indicated by the potential difference ($\Delta V$) between the anodic and cathodic peaks. For the Li‖NCM@TBA cell, the initial cycling pattern shows a narrower potential interval (0.30 V) than that for the Li‖NCM cell (0.34 V). These results indicate that the electrochemical performance of NCM@TBA is better than that of NCM, particularly, in the reversibility and electrochemical polarization of the electrode reaction.

In situ XRD was performed to further investigate the impact of the organic-modified layer on the volume and phase transitions of the NCM cathode during charge and discharge. The cells were tested in the voltage range of 2.80–4.30 V (vs. Li/$Li^+$) at a current of 0.2 C and 25 °C, and the contour maps of (003) reflections of the NCM and NCM@TBA cathodes are presented in Fig. S7 in Supplymentary Material and summarized in Figs. 4a and 4b. Upon $Li^+$ deintercalation, owing to the increased electrostatic repulsion between O slabs, the lattice tends to expand, leading to the shift of diffraction peaks. Thus, when the charge voltage is increased from the open-circuit potential to 4.00 V, the (003) peak gradually shifts to lower angles. With the further increase in voltage to 4.30 V, this peak suddenly shifts to higher angles, indicating the rapid lattice contraction along the *c*-axis and the H2→H3 phase transition. This phenomenon is observed in both cathodes, which is nothing but the different peak position and *c*-axis lattice parameter change ($\Delta c$) are observed between them. The change in the peak position for the NCM@TBA cathode (0.48°) is lower than that for the NCM cathode (0.60°). Correspondingly, the calculated $\Delta c$ of the NCM@TBA cathode (0.31) is lower than that of the NCM cathode (0.42), as shown in Fig. 4c.

Additionally, the H2→H3 phase transition activates reactive oxygen within the lattice, leading to the release of lattice oxygen and catalytic electrolyte decomposition at the interface, thereby generating carbon oxide (CO), $CO_2$, hydrogen fluoride, and hydrogen ($H_2$)[30]. To verify this, $CO_2$ release during battery charging was investigated using differential electrochemical mass spectrometry. The testing voltage range was controlled at 2.80–4.30 V with a current density of 0.2 C, followed by a constant volt-

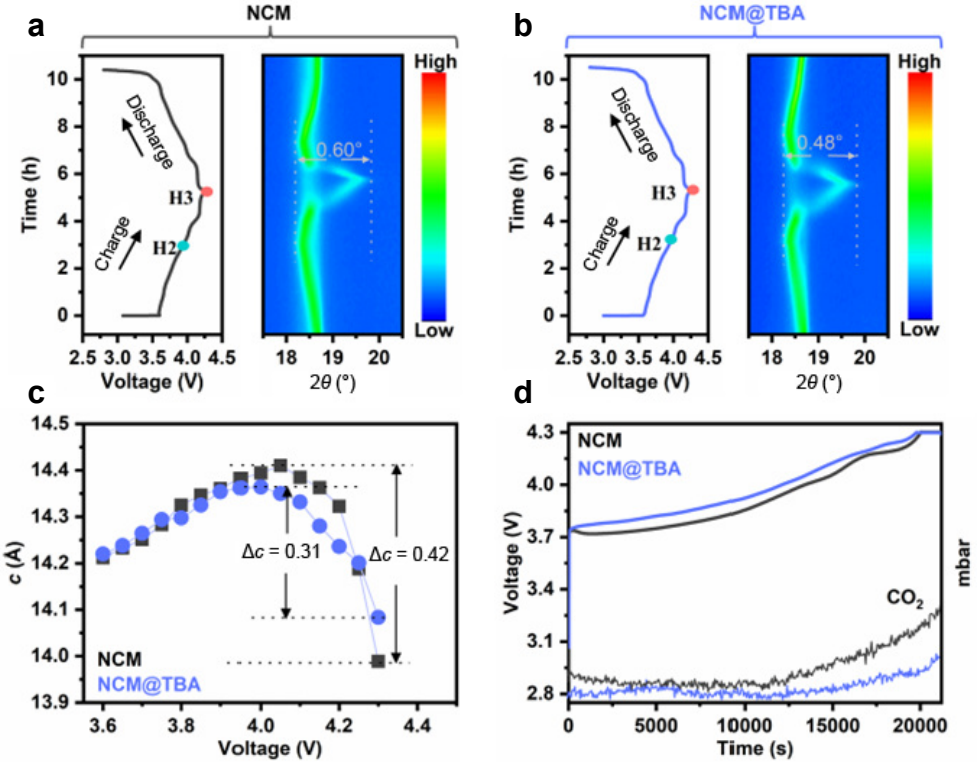


**Figure 4** Structural stability. Contour plots of the *in situ* XRD patterns of the (003) peaks for the Li‖NCM (a) and Li‖NCM@TBA (b) cells and the corresponding charge/discharge curves. (c) Changes in the *c*-axis lattice parameter during delithiation. (d) Differential electrochemical mass spectrometry profiles of the in operando Li‖NCM@TBA cell to confirm gas evolution during charging.

age of 4.30 V for 0.5 h, where the high-voltage state was generally considered the key condition for deep gas release. As shown in Fig. 4d, in the Li‖NCM cell, $CO_2$ production increases with the depth of charge, accompanied by a sharp rise during the constant voltage period. In contrast, the Li‖NCM@TBA cell exhibits considerably lower $CO_2$ release throughout charging, even at the constant voltage. Therefore, these results indicate that the proposed organic modification alleviated the unfavorable H2→H3 phase transition and the strong intergranular strain, preserved the structural stability of the cathode material during cycling, and limited gas evolution, greatly improving the safety and electrochemical performance of the battery.

In postmortem studies, the electrodes cycled for 200 cycles were characterized using XRD, SEM, and TOF-SIMS to assess the protective effect of the proposed organic modification. As shown in Fig. 5a, the intensities of the (003) and (104) peaks for the NCM cathode are notably lower after cycling, with the adjacent sub-peaks almost vanishing. Whereas, the NCM@TBA cathode maintains the appropriate (003)/(104) ratio and shows a negligible decrease in the intensity of these peaks after cycling, indicating the preserved layered structure. Furthermore, the SEM images of the cathodes after cycling also reveal some conspicuous differences. Specifically, many different-sized holes and severe cracks are observed in the NCM granules (Fig. 5b and Fig. S8a in Supplementary Material), leading to the extremely rough surface, which undoubtedly formed owing to the volume changes and electrolyte erosion during battery charge and discharge[31,32]. In contrast, the surface of the NCM@TBA secondary particles is smooth, with unchanged packaging of the primary particles (Fig. 5c and Fig. S8b in Supplementary Material). These results suggest that the proposed organic modification can mitigate volume changes and cracking. This not only enhances the structural stability of the cathode material but also improves the interfacial compatibility between the electrode and the electrolyte, resulting in the suppression of the parasitic reactions with the electrolyte and prolonged battery lifespan.

Furthermore, TOF-SIMS revealed the inhibition of electrolyte decomposition. Based on the 3D surface reconstructions, after 200 cycles, NCM granules are

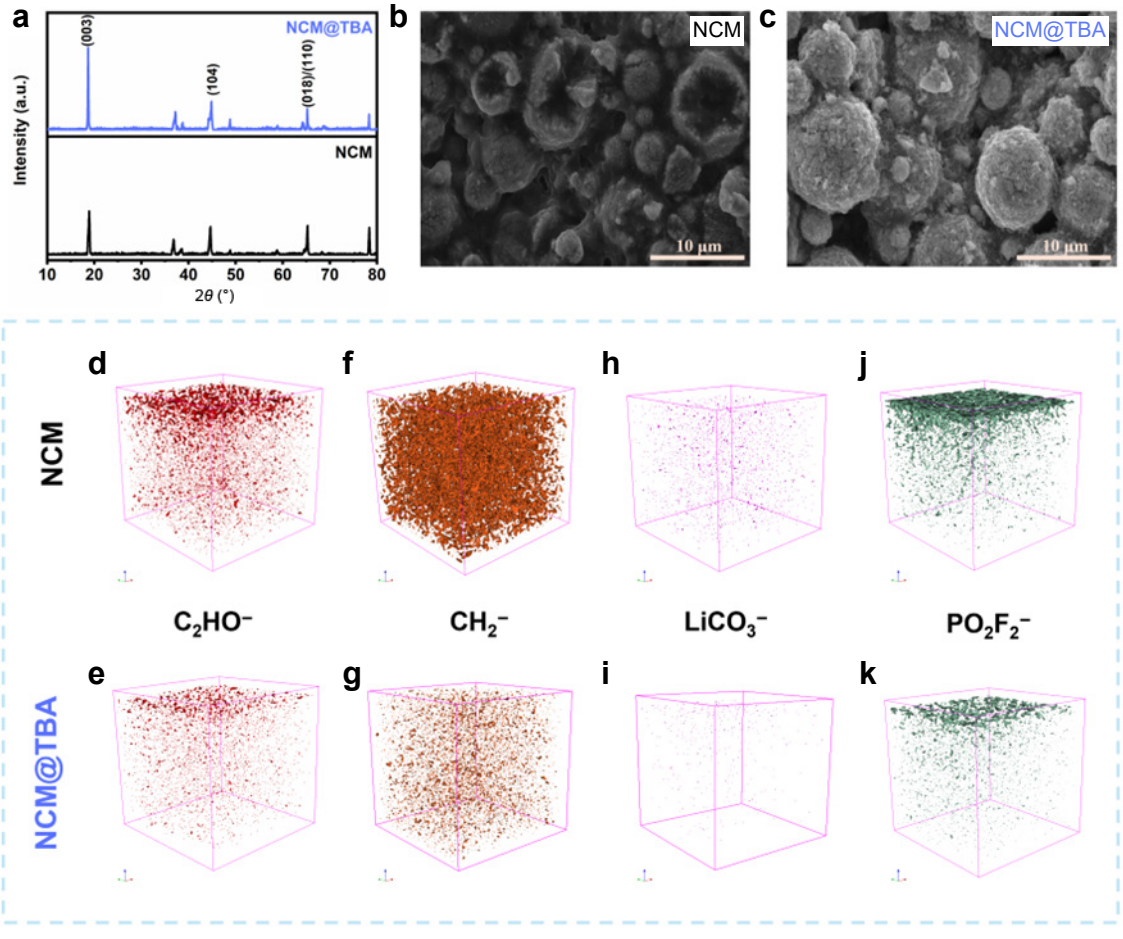


**Figure 5** Electrode characterization after cycling. XRD patterns(a) and SEM images (b, c) of the NCM and NCM@TBA electrodes after 200 cycles. The 3D reconstructions of $C_2HO^-$ (d, e), $CH_2^-$ (f, g), $LiCO_3^-$ (h, i), and $PO_2F_2^-$ (j, k) in the NCM and NCM@TBA cathodes after 200 cycles.

densely covered with $C_2HO^-$ (Fig. 5d), with the density of the distribution gradually decreasing from the surface to the inside. Additionally, the $CH_2^-$ signal is particularly strong in the unmodified sample (Fig. 5f). The two species are known to be the decomposition products of the carbonate solvent and the causes of the interface thickening/accumulation[33–35]. Nevertheless, their contents are low in the cycled NCM@TBA cathode (Figs. 5e and 5g), creating no obstacles to $Li^+$ transfer at the interface[36,37]. This is consistent with the lower interfacial impedance in the EIS spectrum of NCM@TBA. Furthermore, the content of $LiCO_3^-$ on the surface of NCM@TBA is considerably lower than that in the bulk of NCM particles after cycling (Figs. 5h and 5i), demonstrating that the proposed organic modification can reduce and consume Li impurities. The contents of salt byproduct, i.e. $PO_2F_2^-$, on the surfaces of the NCM and NCM@TBA cathodes also notably differ. For the NCM cathode, strong $PO_2F_2^-$ signals are observed on the upper surface (Fig. 5j), indicating serious salt decomposition. This is not observed in the NCM@TBA cathode, where weak and sparse signals are detected (Fig. 5k). Additionally, the signals of $SO_3^-$, $SO_2^-$, $BO_3^-$, $BO_2^-$, and $SO_2F^-$ are uniform for the NCM@TBA cathode (Fig. S9 in Supplementary Material). These B- and S-containing components reveal the protective effect of the organic-modified layer, originating from the neutralization of RLCs by 3-TBA and enhanced compatibility between the electrolyte and the cathode. Thus, the proposed facile organic modification inhibited electrolyte decomposition and improved the electrode/electrolyte interfacial stability and the structural integrity of the material, thereby enhancing battery performance.

## 4 Conclusion

In summary, we proposed a facile strategy for the modification of the surface of the NCM cathode material with 3-TBA. This organic modification improved the structural, chemical, and cycling stabilities of the cathode material and extended its lifespan by suppressing anisotropic volume changes in the lattice during cycling and ensuring rapid $Li^+$ diffusion. Furthermore, the proposed organic modification effectively inhibited the generation of $CO_2$ gas under high-voltage conditions and the side reactions at the electrode/electrolyte interface, thereby considerably improving the safety of the battery and reducing its internal resistance. Owing to these improvements, the cell with the modified cathode, NCM@TBA||Li, showed only 16.66% capacity loss after 200 charge–discharge cycles at 1.0 C and a specific capacity of 162.00 $mAh \cdot g^{-1}$ during charge/discharge at 10.0 C. This facile organic modification strategy neutralizes residual alkali on the surface of the cathode material, forming a thin and uniform interface, thus offering a promising approach for the rational design of advanced high-nickel layered oxide cathode materials for high-performance $Li^+$ batteries.

## Acknowledgements

None.

## Author contribution statement

Chao Zhao is responsible for conceptualization, data curation, formal analysis, investigation, methodology, visualization, and writing original draft. Xiangshao Yin is responsible for resources, software, and validation. Yuanyuan Huang is responsible for software. Xinyu Zhang is responsible for validation. Weihong Jiang is responsible for validation. Zhuo Zhou is responsible for software. Wenhui Tu is responsible for visualization. Xianshu Wang is responsible for conceptualization, data curation, formal analysis, funding acquisition, investigation, methodology, project administration, resources, visualization, and writing—review and editing. Ding Wang is responsible for funding acquisition, resources, supervision. Jianguo Duan is responsible for funding acquisition and resources. All the authors have approved the final manuscript.

## Data availability

The data that support the findings of this study are available from the corresponding author upon reasonable request.

## Declaration of competing interest

All the contributing authors report no conflicts of interest in this work.

## Funding

This work is granted by the Yunnan Fundamental Research Projects (Grant Nos. 202501AT070298, 202401AU070163, and 202401AT070368), the National Natural Science Foundation of China (Grant No. 52162030), the Yunnan Major Scientific and Technological Projects (Grant No. 202202AG 050003), the Yunnan Engineering Research Center Innovation Ability Construction and Enhancement Projects (Grant No. 2023-XMDJ-00617107), the University Service Key Industry Project of Yunnan Province (Grant No. FWCY-ZD2024005), the Yunnan Thousand Talents Program for Young Talents (Grant No. KKS2202052001), the Scientific Research Foundation of Kunming University of Science and Technology (Grant No. 20220122), and the Analysis and Testing Foundation of Kunming

University of Science and Technology (Grant No. 2023T20220122).

## Use of AI statement

None.

**Electronic Supplementary Material**: Supplementary material is available in the online version of this article at https://doi.org/10.26599/EMD.2025.9370056.

## References


[1] Zhou, T., Yu, X. R., Li, F., Zhang, J. W., Liu, B. W., Wang, L. L., Yang, Y., Hu, Z. W., Ma, J., Li, C., et al. (2023). Bulk oxygen release inducing cyclic strain domains in Ni-rich ternary cathode materials. *Energy Storage Mater.* 55, 691–697.

[2] Cho, D. H., Jo, C. H., Cho, W., Kim, Y. J., Yashiro, H., Sun, Y. K., Myung, S. T. (2014). Effect of residual lithium compounds on layer Ni-rich $Li[Ni_{0.7}Mn_{0.3}]O_2$. *J. Electrochem. Soc.* 161, A920–A926.

[3] Liu, W., Oh, P., Liu, X. E., Lee, M. J., Cho, W., Chae, S., Kim, Y., Cho, J. (2015). Nickel-rich layered lithium transition-metal oxide for high-energy lithium-ion batteries. *Angew. Chem. Int. Ed.* 54, 4440–4457.

[4] Chu, B. B., Li, G. X., You, L. Z., Huang, T., Liu, M. M., Yu, A. S. (2021). Enhancing the air stability of $LiNi_{0.6}Co_{0.2}Mn_{0.2}O_2$ cathode through $WO_3/Li_2WO_4$ surface modification. *J. Power Sources* 514, 230605.

[5] Zhou, Y. F., Hu, Z. Y., Huang, Y. H., Wu, Y. J., Hong, Z. J. (2021). Effect of solution wash on the electrochemical performance of $LiNi_{0.8}Co_{0.1}Mn_{0.1}O_2$ cathode materials. *J. Alloys Compd.* 888, 161584.

[6] Xu, S., Du, C. Y., Xu, X., Han, G. K., Zuo, P. J., Cheng, X. Q., Ma, Y. L., Yin, G. P. (2017). A mild surface washing method using protonated polyaniline for Ni-rich $LiNi_{0.8}Co_{0.1}Mn_{0.1}O_2$ material of lithium ion batteries. *Electrochim. Acta* 248, 534–540.

[7] Yang, S. D., Fan, Q. L., Shi, Z. C., Liu, L. Y., Liu, J., Ke, X., Liu, J. P., Hong, C. Y., Yang, Y., Guo, Z. P. (2019). Superior stability secured by a four-phase cathode electrolyte interface on a Ni-rich cathode for lithium ion batteries. *ACS Appl. Mater. Interfaces* 11, 36742–36750.

[8] Chen, Z., Nguyen, H. D., Zarrabeitia, M., Liang, H. P., Geiger, D., Kim, J. K., Kaiser, U., Passerini, S., Iojoiu, C., Bresser, D. (2021). Lithium phosphonate functionalized polymer coating for high-energy $Li[Ni_{0.8}Co_{0.1}Mn_{0.1}]O_2$ with superior performance at ambient and elevated temperatures. *Adv. Funct. Mater.* 31, 2105343.

[9] Zhang, W. J., Yuan, C. H., Zhu, J. F., Jin, T., Shen, C., Xie, K. Y. (2023). Air instability of Ni-rich layered oxides—A roadblock to large scale application. *Adv. Energy Mater.* 13, 2202993.

[10] Yang, T. H., Zhang, K., Zuo, Y. X., Song, J., Yang, Y. L., Gao, C., Chen, T., Wang, H. C., Xiao, W. K., Jiang, Z. W., et al. (2024). Ultrahigh-nickel layered cathode with cycling stability for sustainable lithium-ion batteries. *Nat. Sustain.* 7, 1204–1214.

[11] Seong, W. M., Cho, K. H., Park, J. W., Park, H., Eum, D., Lee, M. H., Kim, I. S. S., Lim, J., Kang, K. (2020). Controlling residual lithium in high-nickel (>90%) lithium layered oxides for cathodes in lithium-ion batteries. *Angew. Chem. Int. Ed.* 59, 18662–18669.

[12] Horner, J. S., Whang, G., Ashby, D. S., Kolesnichenko, I. V., Lambert, T. N., Dunn, B. S., Talin, A. A., Roberts, S. A. (2021). Electrochemical modeling of GITT measurements for improved solid-state diffusion coefficient evaluation. *ACS Appl. Energy Mater.* 4, 11460–11469.

[13] Deiss, E. (2005). Spurious chemical diffusion coefficients of $Li^+$ in electrode materials evaluated with GITT. *Electrochim. Acta* 50, 2927–2932.

[14] Hua, W. B., Schwarz, B., Azmi, R., Müller, M., Dewi Darma, M. S., Knapp, M., Senyshyn, A., Heere, M., Missyul, A., Simonelli, L., et al. (2020). Lithium-ion (de)intercalation mechanism in core–shell layered $Li(Ni,Co,Mn)O_2$ cathode materials. *Nano Energy* 78, 105231.

[15] Zuo, W. H., Luo, M. Z., Liu, X. S., Wu, J., Liu, H. D., Li, J., Winter, M., Fu, R. Q., Yang, W. L., Yang, Y. (2020). Li-rich cathodes for rechargeable Li-based batteries: Reaction mechanisms and advanced characterization techniques. *Energy Environ. Sci.* 13, 4450–4497.

[16] Xia, Y., Zheng, J. M., Wang C. M., Gu, M. (2018). Designing principle for Ni-rich cathode materials with high energy density for practical applications. *Nano Energy* 49, 434–452.

[17] Stankovich, S., Dikin, D. A., Piner, R. D., Kohlhaas, K. A., Kleinhammes, A., Jia, Y. Y., Wu, Y., Nguyen, S. T., Ruoff, R. S. (2007). Synthesis of graphene-based nanosheets via chemical reduction of exfoliated graphite oxide. *Carbon* 45, 1558–1565.

[18] Hartmann, L., Pritzl, D., Beyer, H., Gasteiger, H. A. (2021). Evidence for $Li^+/H^+$ exchange during ambient storage of Ni-rich cathode active materials. *J. Electrochem. Soc.* 168, 070507.

[19] Zhong, Y. X., Li, C. M., Xu, G. B., Xu, C. Y., Dong, J., Liu, D. Y., Lu, D. C., You, J. Y., Gao, C. M., Song, Q. L. (2022). Collaborative strengthening by multi-functional molecule 3-thiophenboric acid for efficient and stable planar perovskite solar cells. *Chem. Eng. J.* 436, 135134.

[20] Li, Z. F., Lin, X. Y., Zhou, H. B., Xing, L. D., Lan, G. Y., Zhang, W. G., Chen, J. W., Liu, M. Z., Huang, Q. M., Li, W. S. (2020). Stabilizing the interphasial layer of Ni-rich cathode and graphite anode for lithium ion battery with multifunctional additive. *J. Power Sources* 467, 228343.

[21] Ren, W. H., Huang, Y., Li, S. S., Gan, J. Y., Yang, J., Li, X., Wang, M. S., Cao, H. J. (2021). 3-Thiopheneboronic acid: An effective additive for regulation on electrode/electrolyte interphase of lithium metal battery with high-loading cathode. *Electrochim. Acta* 386, 138485.

[22] Dai, Z. S., Wang, J. H., Zhao, H. L., Bai, Y. (2022). Surface coupling between mechanical and electric fields empowering Ni-rich cathodes with superior cyclabilities for lithium-ion batteries. *Adv. Sci.* 9, 2200622.

[23] Zhang, X. Y., Xu, J., Liu, X. T., Cheng, F. Y., Wei, P., Xu, Y., Sun, S. X., Lin, H., Shen, Y., Li, Q., et al. (2022). Building a stabilized structure from surface to bulk of Ni-rich cathode for enhanced electrochemical performance. *Energy Storage Mater.* 47, 87–97.

[24] Han, J. G., Kim, K., Lee, Y., Choi, N. S. (2019). Scavenging materials to stabilize $LiPF_6$-containing carbonate-based electrolytes for Li-ion batteries. *Adv. Mater.* 31, 1804822.

[25] Li, Y., Chen, J. X., Cai, P. W., Wen, Z. H. (2018). An electrochemically neutralized energy-assisted low-cost acid-alkaline electrolyzer for energy-saving electrolysis hydrogen generation. *J. Mater. Chem. A* 6, 4948–4954.

[26] Ye, J. C., Lai, Y. W., Huang, X. H., Chang, Z. X., Chung, Y. H., Shu, C. M. (2024). Development of the electrolyte in lithium-ion battery: A concise review on its thermal hazards. *J. Therm. Anal. Calorim.* 149, 11293–11312.

[27] Liu, W., Li, X. F., Xiong, D. B., Hao, Y. C., Li, J. W., Kou, H. R., Yan, B., Li, D. J., Lu, S. G., Koo, A., et al. (2018). Significantly improving cycling performance of cathodes in lithium ion batteries: The effect of $Al_2O_3$ and $LiAlO_2$ coatings on $LiNi_{0.6}Co_{0.2}Mn_{0.2}O_2$. *Nano Energy* 44, 111–120.

[28] Liu, J. D., Wu, Z. H., Yu, M., Hu, H. L., Zhang, Y. D., Zhang, K., Du, Z. X., Cheng, F. Y., Chen, J. (2022). Building homogenous $Li_2TiO_3$ coating layer on primary particles to stabilize Li-rich Mn-based cathode materials. *Small* 18, 2106337.

[29] Liu, Y. J., Zeng, T. Y., Li, G. T., Wan, T., Li, M. Y., Zhang, X. Y., Li, M. Q., Su, M. R., Dou, A. C., Zeng, W. S., et al. (2022). The surface double-coupling on single-crystal $LiNi_{0.8}Co_{0.1}Mn_{0.1}O_2$ for inhibiting the formation of intragranular cracks and oxygen vacancies. *Energy Storage Mater.* 52, 534–546.

[30] Wandt, J., Freiberg, A. T. S., Ogrodnik, A., Gasteiger, H. A. (2018). Singlet oxygen evolution from layered transition metal oxide cathode materials and its implications for lithium-ion batteries. *Mater. Today* 21, 825–833.

[31] Lin, T. E., Seaby, T., Hu, Y. X., Ding, S. S., Liu, Y., Luo, B., Wang, L. Z. (2022). Understanding and control of activation process of lithium-rich cathode materials. *Electrochem. Energy Rev.* 5, 27.

[32] Boivin, E., Guerrini, N., House, R. A., Lozano, J. G., Jin, L. Y., Rees, G. J., Somerville, J. W., Kuss, C., Roberts, M. R., Bruce, P. G. (2021). The role of Ni and Co in suppressing O-loss in Li-rich layered cathodes. *Adv. Funct. Mater.* 31, 2003660.

[33] Hu, G. L., Yang, Z. L., Zhang, X. X., Liu, Y. C., Lin, Y. S., Chen, S. J., Chen, Y. Q., Sa, B. S., Zhang, Y. N. (2024). Strongly solvating triglyme-based electrolyte realizes stable lithium metal batteries at high-voltage and high-temperature. *Energy Storage Mater.* 69, 103402.

[34] Groß, A. (2018). Fundamental challenges for modeling electrochemical energy storage systems at the atomic scale. *Top. Curr. Chem.* 376, 17.

[35] Kim, S., Huang, H. Y. S. (2016) Mechanical stresses at the cathode–electrolyte interface in lithium-ion batteries. *J. Mater. Res*. 31, 3506–3512.

[36] Huang, Z. X., Liu, X., Zheng, Y., Wang, Q., Liu, J. W., Xu, S. M. (2023). Boosting efficient and low-energy solid phase regeneration for single crystal $LiNi_{0.6}Co_{0.2}Mn_{0.2}O_2$ via highly selective leaching and its industrial application. *Chem. Eng. J.* 451, 139039.

[37] Zhu, Z., Wang, H., Li, Y., Gao, R., Xiao, X. H., Yu, Q. P., Wang, C., Waluyo, I., Ding, J. X., Hunt, A., et al. (2020). A surface se-substituted $LiCo[O_{2-\delta}Se_{\delta}]$ cathode with ultra-stable high-voltage cycling in pouch full-cells. *Adv. Mater.* 32, 2005182.